

The Gaia-ESO Survey: processing of the FLAMES-UVES spectra[★]

G. G. Sacco¹, L. Morbidelli¹, E. Franciosini¹, E. Maiorca¹, S. Randich¹, A. Modigliani², G. Gilmore³, M. Asplund⁴, J. Binney⁵, P. Bonifacio⁶, J. Drew⁷, S. Feltzing⁸, A. Ferguson⁹, R. Jeffries¹⁰, G. Micela¹¹, I. Negueruela¹², T. Prusti¹³, H.-W. Rix¹⁴, A. Vallenari¹⁵, E. Alfaro¹⁶, C. Allende Prieto^{17,18}, C. Babusiaux⁶, T. Bensby¹⁹, R. Blomme²⁰, A. Bragaglia²¹, E. Flaccomio¹¹, P. Francois⁶, N. Hambly²², M. Irwin³, S. Koposov³, A. Korn²³, A. Lanzafame²⁴, E. Pancino^{21,25}, A. Recio-Blanco²⁶, R. Smiljanic^{27,29}, S. Van Eck²⁸, N. Walton³, M. Bergemann³, M. T. Costado¹⁶, P. de Laverny²⁶, U. Heiter²³, V. Hill²⁶, A. Hourihane³, R. Jackson¹⁰, P. Jofre³, J. Lewis³, K. Lind³, C. Lardo²¹, L. Magrini¹, T. Masseron³, L. Prisinzano¹¹, and C. Worley³

(Affiliations can be found after the references)

Received ; accepted

ABSTRACT

The Gaia-ESO Survey is a large public spectroscopic survey that aims to derive radial velocities and fundamental parameters of about 10^5 Milky Way stars in the field and in clusters. Observations are carried out with the multi-object optical spectrograph FLAMES, using simultaneously the medium resolution ($R \sim 20,000$) GIRAFFE spectrograph and the high resolution ($R \sim 47,000$) UVES spectrograph. In this paper, we describe the methods and the software used for the data reduction, the derivation of the radial velocities, and the quality control of the FLAMES-UVES spectra. Data reduction has been performed using a workflow specifically developed for this project. This workflow runs the ESO public pipeline optimizing the data reduction for the Gaia-ESO Survey, performs automatically sky subtraction, barycentric correction and normalisation, and calculates radial velocities and a first guess of the rotational velocities. The quality control is performed using the output parameters from the ESO pipeline, by a visual inspection of the spectra and by the analysis of the signal-to-noise ratio of the spectra. Using the observations of the first 18 months, specifically targets observed multiple times at different epochs, stars observed with both GIRAFFE and UVES, and observations of radial velocity standards, we estimated the precision and the accuracy of the radial velocities. The statistical error on the radial velocities is $\sigma \sim 0.4 \text{ km s}^{-1}$ and is mainly due to uncertainties in the zero point of the wavelength calibration. However, we found a systematic bias with respect to the GIRAFFE spectra ($\sim 0.9 \text{ km s}^{-1}$) and to the radial velocities of the standard stars ($\sim 0.5 \text{ km s}^{-1}$) retrieved from the literature. This bias will be corrected in the future data releases, when a common zero point for all the setups and instruments used for the survey will be established.

Key words. Methods:data analysis, Techniques: spectroscopic, Techniques: radial velocities, Surveys, Stars:general

1. Introduction

The Gaia-ESO Survey is a large public spectroscopic survey aimed at deriving radial velocities (RVs), stellar parameters, and abundances of about 10^5 Milky Way stars in the field and in clusters (Gilmore et al. 2012; Randich & Gilmore 2013). The observations started at the end of 2011 and are expected to last for about 5 years.

The observations are carried out with the multi-object optical spectrograph FLAMES (Pasquini et al. 2002). This instrument is located at the Nasmyth focus of the UT2 at the Very Large Telescope (VLT) and is composed of a robotic fibre positioner equipped with two sets of 132 and 8 fibres, which feed the optical spectrographs GIRAFFE ($R \sim 20,000$) and UVES ($R \sim 47,000$), respectively. A good fraction of the spectra (~ 3500 from GIRAFFE and ~ 300 from UVES) observed during the first six months (December 2011-June 2012) have been released and are available at the webpage http://www.eso.org/sci/observing/phase3/data_releases.html.

Twenty working groups (WGs) are in charge of the workflow, which includes all steps from the selection of the targets

to be observed to the derivation of the stellar parameters. This paper describes the methods and software used for the reduction of the FLAMES-UVES spectra and for the derivation of RVs and rotational velocities projected along the line of sight ($v \sin i$). We will focus on the spectra gathered during the first 18 months of observations (from December 2011 to June 2013). Whilst all other steps of the workflow are performed in a distributed fashion, namely several nodes analyse the same data, and the results are finally made homogeneous by the WG coordinators, the work discussed in this paper has been carried out by one team based at INAF-Osservatorio Astrofisico di Arcetri.

The content of the paper is summarized as follows: in Sect. 2 we briefly describe the target sample and the observations; in Sect. 3 we explain the procedures used for the data reduction of the FLAMES-UVES spectra; in Sect. 4 we describe the methods used to derive RVs and $v \sin i$; in Sect. 5 we summarize our quality control procedure; in Sect. 6 we list the final products of our WG; and in Sect. 7 a summary of the paper is provided.

2. Target sample and observations

The target sample of the Gaia-ESO Survey includes a large variety of stars (dwarfs and giants) with spectral types ranging from O to M and expected metallicities $[\text{Fe}/\text{H}]$ from about -2.5 to $+0.5$

[★] Based on observations made with the ESO/VLT, at Paranal Observatory, under program 188.B-3002 (The Gaia-ESO Public Spectroscopic Survey)

dex. The setup centered at 580 nm (480-680 nm) is used for all FLAMES-UVES observations with the exception of the early-type stars, that are observed with the setup centered at 520 nm (420-620 nm), and of the targets selected for calibration and testing purposes, which are observed with all FLAMES-UVES setups, including the one centered at 860 nm (760-960 nm).

Typical exposure times of observing blocks (OBs) observed with the 580 setup are either 1200 or 3000 s, with the exception of the targets observed for calibration, especially the very bright ones, that are observed for a very short time to avoid saturation. However, an OB can be repeated multiple times and a target can be included in different OBs, so the time spent on a single target can be longer. Each OB is divided into two separate exposures to help the removal of cosmic rays. A very short exposure including an arc lamp spectrum is executed between the two main exposures to provide a nearly simultaneous calibration of the GIRAFFE observations, with the exception of the observations carried out with the HR21 setup (848-900 nm), which are calibrated using sky emission lines.

Note that the determination of very precise RVs is not the primary goal of the UVES observations and the acquisition of a simultaneous arc lamp spectrum can be performed only losing one science target, so to maximize the number of UVES targets, we perform the wavelength calibration using the arc lamp frame acquired during the day. Usually, all the 8 fibres (6 for the 520 nm setup) are allocated with at least one fibre on an empty position of the sky to allow the subtraction of the sky emission. The FLAMES fibre positioner is equipped with two plates¹, that are both used to reduce observing overheads; in fact, fibres can be positioned on one plate, while the other one is used for observing.

3. Data volume and structure

The survey started on 31 December 2011. All the observations are carried out in Visitor mode and are divided in runs of 5-6 nights, with a monthly frequency. During the first 18 months, we performed 17 observing runs for a total of 87 observing nights. We processed a total of 6971 FLAMES-UVES spectra of 1611 stars, which have been internally released to the WGs in charge of the spectral analysis. All stars have been observed with the 580 setup, while only 27 stars have been observed also with the 860 setup. Due to data reduction problems discussed in the next section, stars observed with the 520 setup have not yet been released.

We organize our data reduction flow on single night basis, namely we use the same set of calibration frames for all the observations carried out during the same night with the same setup and the same plate. A set of calibrations is composed of five bias frames, nine full slit flat-fields, three fibre flat-fields, two frames for the format definition, and one frame for the wavelength calibration. A typical observing night includes 8-10 OBs (~24-30 exposures), which are associated to different sets of calibrations (from one to six), depending on the setups and the plates used for the observations. However, the amount of science frames taken during a night strongly depends on the type of targets and the weather conditions. For the calibrations, we use frames taken in daytime soon after the observing night, with the exception of specific cases, where our quality control identifies a poor quality

of some calibration frames. In these cases we use the calibration frames suitable for our observations, which are closest in time.

4. Data reduction

We process the spectra with a data flow software composed of a combination of public software (i.e. ESO public pipeline, IRAF², Pyraf³) and a set of bash, IDL, and python scripts developed by our team. The whole data flow can be divided into three main parts: a) the reduction of raw frames to produce wavelength-calibrated spectra, which is performed by a set of scripts running the public ESO pipeline (Modigliani et al. 2004; Modigliani & Larsen 2012) within a workflow optimized for the survey observing strategy; b) the basic steps of the data analysis (i.e. sky-subtraction, barycentric correction, normalization and co-adding) and the derivation of RV, $v \sin i$ and binarity flags, which are performed using a set of IDL and IRAF/Pyraf (Tody 1986, 1993) scripts; c) the scientific quality control of the final products.

The FLAMES-UVES data reduction pipeline was originally developed as a MIDAS based pipeline (Mulas et al. 2002) and later ported to ESO Common Pipeline Library. It consists of a chain of seven recipes, which perform the following steps:

- combining raw bias frames into a master bias;
- computing guess tables with order positions on the detector, using a physical model of the instrument and a raw frame which is acquired by illuminating a fibre with a line emission lamp;
- computing a more accurate table with order positions from a raw frame taken with the calibration fibre illuminated by a continuum lamp;
- creating the master slit flat-field frame by combining several long slit exposures taken with a continuum lamp;
- determining the fibre order table and constructing several frames needed to extract a science fibre frame, using input fibre frames obtained by illuminating the fibres with a continuum source;
- determining the wavelength dispersion coefficients and constructing a wavelength calibration table from a frame where all the fibres are illuminated by an arc line calibration lamp;
- extracting the science frame producing the reduced spectra and their variances. The output spectra and variances are given in three different formats: a) single echelle order spectra before the wavelength calibration, b) single echelle order spectra after the wavelength calibration, c) a wavelength calibrated spectrum created by merging all the echelle orders.

It is worth noting that the FLAMES-UVES detector is the mosaic of two CCDs, which cover the redder and the bluer part of the spectral format. The ESO pipeline processes data from each CCD independently, and provides for each target two output files, each covering half of the full wavelength range of the setup. We keep the two spectral ranges separated for the whole data flow, so all the subsequent steps of the spectra processing described in this paper are performed independently for each spectral range. In the rest of the paper, we will refer to the two spectral ranges as lower and upper spectrum.

² IRAF is distributed by the National Optical Astronomy Observatories, which are operated by the Association of Universities for Research in Astronomy, Inc., under cooperative agreement with the National Science Foundation

³ Pyraf is a product of the Space Telescope Science Institute, which is operated by AURA for NASA.

¹ Since September 2012, one of the fibre on plate 2 has been dismissed due to a hardware problem. So on this plate we can allocate only seven targets including the sky.

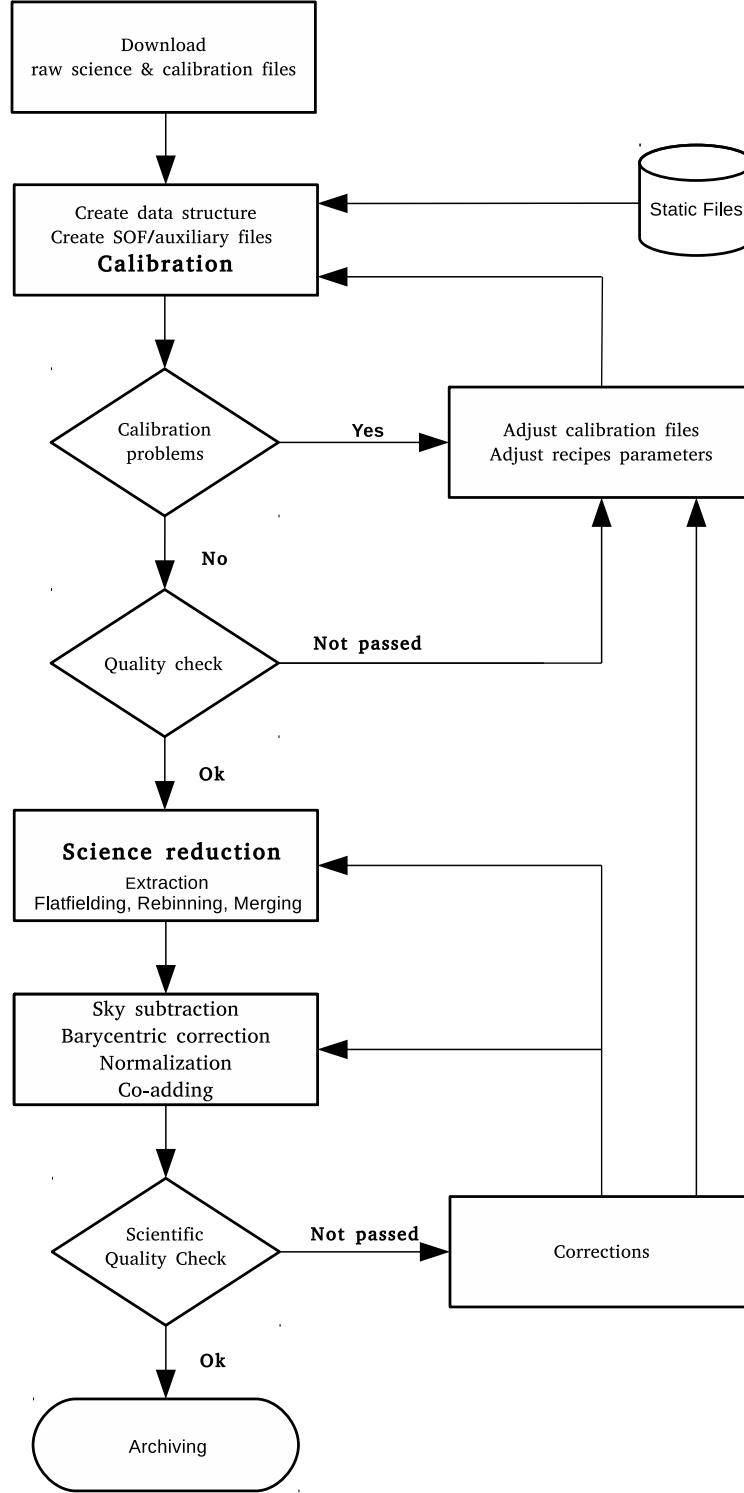


Fig. 1. Flowchart describing the workflow for the reduction of the FLAMES-UVES spectra for the Gaia-ESO Survey.

These recipes can be executed via the command line interface ESOREX, the graphic interface Gasgano or the Reflex workflow. However, ESOREX requires additional software to classify the files and to organise the workflow, while Gasgano and Reflex are designed for interactive data reduction, and thus are not the best choice reduction of very large datasets. There-

fore, we built a workflow to manage efficiently the ESOREX based data reduction process and perform the quality control on the calibrations. Specifically, our workflow performs automatically the following operations: a) classifies the raw data files in categories (e.g. science, bias, flat-field and so on); b) groups the calibration raw files in sets of calibration frames, according to

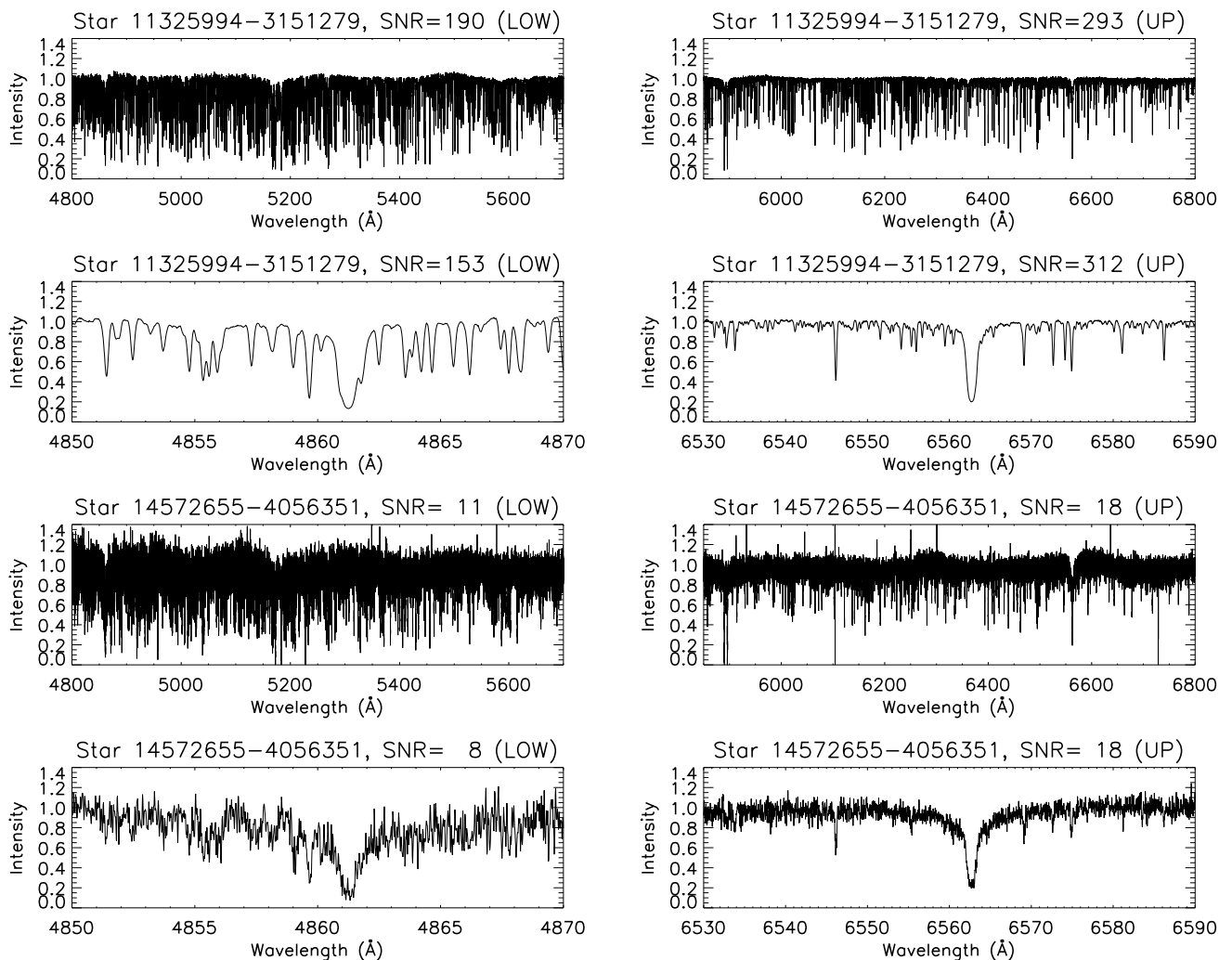


Fig. 2. Examples of co-added and normalised spectra of the Gaia-ESO Survey. The panels in the first two rows show different wavelength ranges of a spectrum with high signal-to-noise ratio (star 11325994-3151279). Specifically, the first row shows the entire lower (left panel) and upper (right panel) spectra, while the second row shows two smaller portions of the spectrum around the H β (left panel) and H α (right panel) lines. The panels in the last two rows show the same ranges of a spectrum with low signal-to-noise ratio (star 14572655-4056351). On the top of each panel is reported the median of the signal-to-noise ratio per pixel for the spectral range plotted in the panel.

the setups and the plates used for the observations; c) executes the cascade of recipes for each set of calibration frames; d) associates the output of the calibration recipes to each science raw frame; e) executes the last recipe on each science raw file; f) produces tables and plots for quality control.

A schematic flowchart of the workflow is shown in Fig. 1. A script starts the calibration procedure by executing consecutively the set of recipes, using the ESOREX command line interface. At the end of the calibration phase the output files are checked in order to detect problems and assess quality. If quality problems are detected (a detailed description of quality control procedure and of the quality issues affecting the data is given in Sect. 6) or some recipes did not complete successfully, it is necessary to check where the problem originates, fix it by selecting different values of the key parameters or by choosing different calibration files, and start again the workflow. Only after all calibrations are reduced properly, we run the recipe to reduce the science frame.

Since the first period of observations, we experienced problems with the wavelength calibration and the definition of the order positions of the frames acquired with the 520 setup. For this reason, data taken with the setup at 520 nm are not part of

the first releases. However, the ESO data reduction team recently solved this issue and released a new version of the pipeline in November 2013. Several tests have shown that the quality of the spectra reduced with this new pipeline are equivalent for all setups. Therefore, all spectra will be delivered in the next release.

After all the recipes of the ESO pipeline have been executed and the quality of the calibration has been assessed we perform the following operations:

1. We subtract the sky background spectrum from the stellar spectra. The sky background spectrum is usually acquired by one fibre pointing toward an empty position of the field of view. If more than one fibre is used to sample the sky emission, we compute the median of the sky emission spectra (or the average if they are only two).
2. We shift all the sky-subtracted spectra to an heliocentric reference frame, using the IRAF task RVCORRECT to calculate the velocity shift due to the Earth rotation, the motion of the Earth center about the Earth-Moon barycenter and the motion of the Earth-Moon barycenter about the center of the Sun.

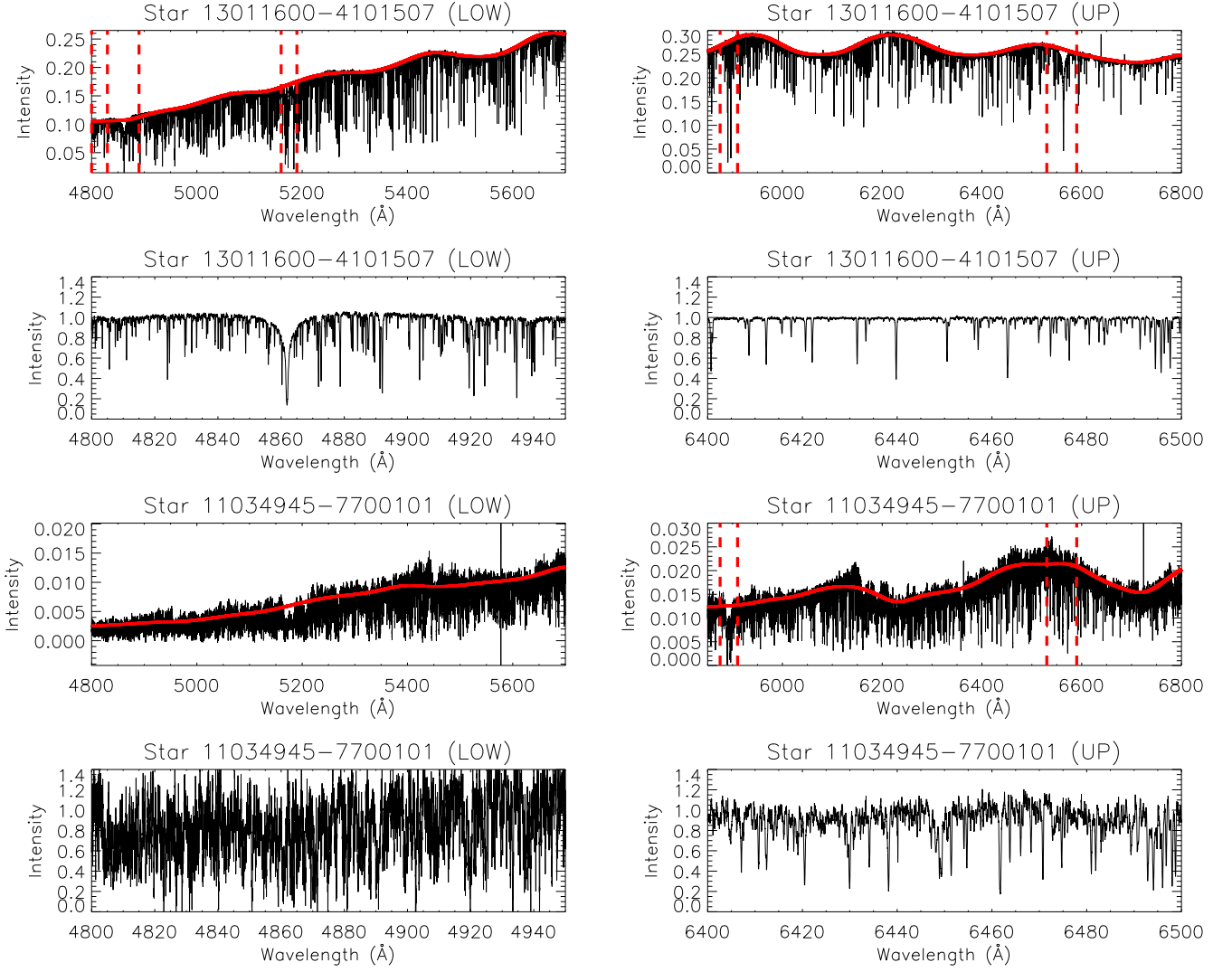


Fig. 3. Examples of the results obtained with the normalisation procedure used for processing the spectra of the Gaia-ESO survey. The four top panels show a typical spectrum (star 13011600-4101507), while the four bottom panels show one of the case (star 1103495-7700101) when our procedure does not perform efficiently. The continuous red lines overplotted on the spectra before the normalisation show the profile of the continuum calculated by the pipeline, while the vertical dashed lines indicate the wavelength intervals masked to avoid overnormalisation of strong lines.

3. After the end of each run, we co-add and store in a single file all the spectra from different exposures of the same OB and/or different OBs with the same configuration, which have been observed during the same night. Very short exposures taken for the wavelength calibration of the GIRAFFE spectra are not co-added. Before each data release, we produce a final spectrum and a single final file for each star. This final spectrum is the sum of all the spectra of the same star acquired during the whole survey. Note that a specific target can be part of different OBs observed in different nights or different runs, so some of the final spectra are the sum of multi-epoch observations. As explained in more detail in the next section, all the candidate binaries are flagged. We do not perform the subtraction of the telluric absorption features before co-adding, therefore, when strong telluric features affect multi-epoch observations, the final co-added spectrum may be affected by multiple telluric features. To handle this problem and any other issues related to the variability of the spectra, we include in the file with the final co-added

spectrum also the original single-epoch spectra, before co-adding.

4. We normalise the merged spectra by dividing them by a function, which describes the stellar continuum emission convolved with the FLAMES-UVES instrumental response. To derive this function, we divide the spectrum in 30 bins, compute the median in each bin, and then fit the obtained values with a spline function, using an iterative sigma-clipping to remove absorption and emission features. Strong lines (e.g. Balmer lines) are masked before the calculation of the continuum function to avoid over-normalisation. Some examples of spectra before and after the normalisation and of the function used to define the continuum are shown in Fig. 3. As shown in the four bottom panels of the figure, our procedure may not work for very noisy spectra and late-type stars. Furthermore, in many cases the procedure for the normalisation of the spectra needs to be tuned on the basis of method used for the spectral analysis. Therefore, both spectra before and after the normalisation are internally released, and the teams

performing the spectral analysis can re-normalize them, before deriving stellar parameters and abundances.

5. We calculate RVs, $v \sin i$ and associated flags to assess the quality of these measurements, as described in the next section.

The first three steps discussed above (sky subtraction, helio-centric correction and co-adding) are applied to both the single orders and the merged spectra, while only the merged spectra are normalised. Variances of the spectra are propagated across these steps following basic error propagation theory. As shown in Fig. 1, after these four steps have been completed, we perform a scientific quality control (see section 6).

5. Radial velocities and rotational broadening

We derive the stellar RVs by cross-correlating each spectrum with a grid of synthetic template spectra. Our grid is a subsample of the library produced by de Laverny et al. (2012) and is composed of 36 synthetic spectra convolved at the FLAMES-UVES spectral resolution. It covers seven effective temperatures ($T_{\text{eff}} = 3100, 4000, 5000, 6000, 7000, 8000$ K), three surface gravities ($\log(g) = 2.5, 4.0, 5.0$) and two values of metallicities ($[\text{Fe}/\text{H}] = 0.0, -1.0$).

Each spectrum is cross-correlated with all the spectra of the grid, using the IRAF task FXCOR (Fitzpatrick 1993), masking the Balmer lines ($H\alpha$ and $H\beta$) and regions of the spectra with strong telluric lines. To derive the RV, we select the cross-correlation function (CCF) with the highest peak and fit the peak with a Gaussian function to derive its centroid. This procedure fails for early-type stars with an effective temperature above the highest temperature of our grid, which are characterized by the presence of no, or very few, absorption lines other than the Balmer lines. A WG dedicated to the analysis of the early-type stars will provide RVs for these stars, by a best-fitting procedure with an appropriate grid of templates. Details on this procedure will be given in a forthcoming paper.

To estimate the precision of the RVs derived by our pipeline, we used the differences between RVs measured from the lower (RV_L) and upper spectra (RV_U), which are measured independently by the pipeline. Assuming identical uncertainties on RVs from the two wavelength ranges, and since there is no systematic offset between lower and upper spectra ($\text{median}(RV_U - RV_L) = 0.007 \text{ km s}^{-1}$), the statistical error on the RVs derived by our pipeline is $\sigma_{UL} = |RV_U - RV_L| / \sqrt{2}$. The distribution of these empirical errors for the stars observed with the 580 setup⁴ during the first 18 months of the survey is shown in the top panel of Fig. 4. The distribution deviates from a Gaussian due to extended wings associated to a small fraction of spectra which are affected by large errors (e.g., very low signal-to-noise ratio spectra, fast rotators, spectroscopic binaries). Excluding these outliers, the statistical error on RV is equal to the 68th percentile rank of the distribution ($\sigma = 0.18 \text{ km s}^{-1}$).

We use the empirical error based on the RV differences between the upper and lower spectrum to investigate how the precision of the RVs depends on the signal-to-noise ratio (SNR) and $v \sin i$. The middle and bottom panels of Fig. 4 show the empirical error binned by SNR and full width half maximum of the CCF (CCF_{FWHM}), respectively. The latter is correlated

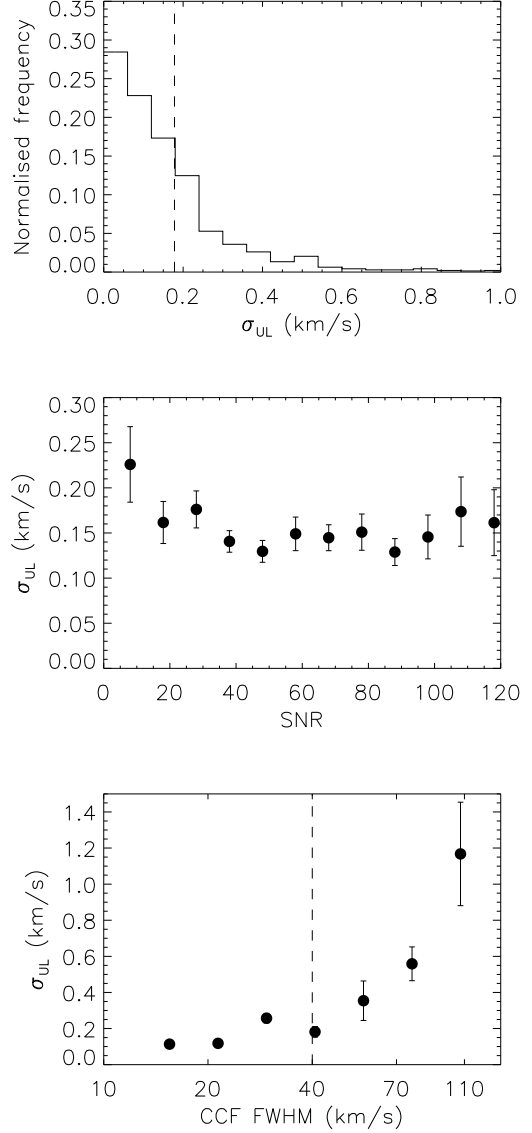


Fig. 4. Empirical estimate of the errors on radial velocities. **Top panel:** the normalised frequency distribution of empirical uncertainties ($\sigma_{UL} \sim |RV_U - RV_L| / \sqrt{2}$) derived from the difference between velocities measured from the upper (RV_U) and lower (RV_L) spectrum of all the stars observed with the 580 setup. The dashed line shows the position of the 68th percentile of the distribution. **Middle and bottom panels:** the same empirical uncertainties binned as a function of the SNR of the spectra (middle panel) and of the full width half maximum of the CCF (bottom panel). Error bars on each bin are equal to $\sigma_{bin} / \sqrt{N_{bin}}$, where σ_{bin} and N_{bin} are the standard deviation and the total number of values for each bin, respectively. The number of values per bin is not constant, but it ranges from ~ 200 (in the central bins, $SNR \sim 40 - 50$) to ~ 50 (bins of the lowest and highest SNR) in the middle plot, and from ~ 900 ($CCF_{FWHM} \sim 20 \text{ km s}^{-1}$) to ~ 20 ($CCF_{FWHM} \sim 110 \text{ km s}^{-1}$) in the bottom plot.

with $v \sin i$ and can be directly measured. A small fraction of RVs ($\sim 3\%$) have been excluded after a sigma-clipping applied to each bin. The error on RV shows almost no dependence on the SNR, while it strongly increases in fast rotators. Specifically, the error is constant for a CCF_{FWHM} smaller than $\sim 40 \text{ km s}^{-1}$ ($v \sin i \sim 15 \text{ km s}^{-1}$) and increases above. Due to the low statistics, it is not possible to determine a relation between the er-

⁴ Since no spectra observed with the 520 setup have been released and only 27 benchmark stars have been observed with the 860 setup, we limit our analysis of the RV precision and accuracy to the spectra observed with the 580 setup.

ror and the CCF_{FWHM} for fast rotators, therefore we include in our products a RV quality flag calculated using the maximum of the CCF and the CCF_{FWHM} . Specifically, we flag all the stars with $CCF_{FWHM} > 40 \text{ km s}^{-1}$ and a maximum of the CCF lower than 0.3. Errors on RVs may also depend on the stellar metallicity [Fe/H]. However, the number of metal-poor stars is not high enough to study the relation between σ_{UL} and [Fe/H]. To obtain a first estimation on this source of error, we calculate the 68th percentile rank of the distribution of σ_{UL} for the metal-poor stars ([Fe/H] < -1.0 dex, 68th rank $\sim 0.24 \text{ km s}^{-1}$) and metal-rich stars ([Fe/H] > +0.1 dex, 68th rank $\sim 0.14 \text{ km s}^{-1}$). The latter is slightly higher suggesting that measurements of RV for metal poor stars are less precise.

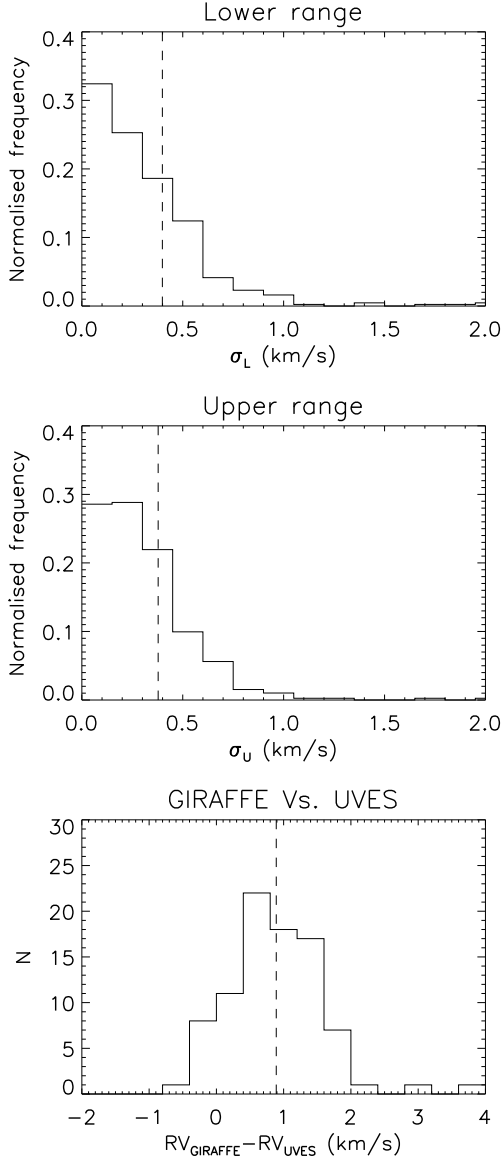


Fig. 5. Errors due to the zero point of wavelength calibration. The top and the middle panels show the normalised frequency distributions of empirical uncertainties ($\sigma \sim |\Delta RV|/\sqrt{2}$) derived from stars observed multiple times in different epochs for the lower and upper wavelength range, respectively. The dashed lines show the position of the 68% percentile. The bottom panel shows the distribution of the differences between radial velocities observed with both the UVES 580 setup and the GIRAFFE HR15N setup. The dashed line shows the position of the median of the differences.

Since the upper and the lower spectrum are calibrated using the same arc lamp, our approach for the error estimate does not take into account the error due to the variations of the zero point of the wavelength calibration. In order to estimate this source of uncertainty, we used spectra of targets observed multiple times in different epochs. The top (lower wavelength range) and middle (upper wavelength range) plots in Fig. 5 show the distributions of an empirical error defined as above ($\sigma = |\Delta RV|/\sqrt{2}$), where $|\Delta RV|$ is the difference between two observations of the same target performed in different nights. The two distributions are much wider than the distribution reported in the top panel of Fig. 4 (the 68th percentile ranks $\sigma_U = 0.38 \text{ km s}^{-1}$ and $\sigma_L = 0.40 \text{ km s}^{-1}$ for the lower and upper ranges, respectively), which proves that the variations of the zero point of the wavelength calibration are the main source of uncertainty. Therefore, we will adopt $\sigma \sim 0.4 \text{ km s}^{-1}$ as typical error for the RVs derived from the FLAMES-UVES spectra⁵ of the Gaia-ESO Survey.

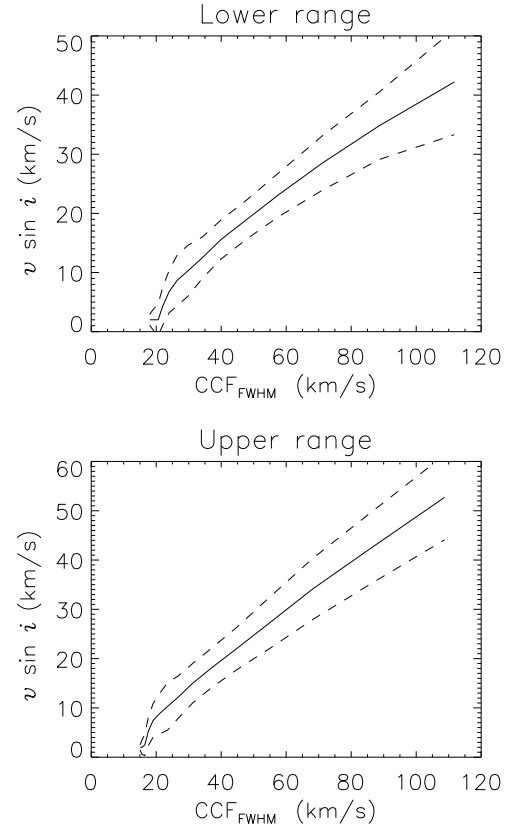


Fig. 6. The continuous line describes the relations between $v \sin i$ and the CCF_{FWHM} used to derive $v \sin i$ from the lower (top panel) and upper wavelength range for the stars observed with the 580 setup. Dashed lines describe the same relations plus/minus the error bars.

To estimate the accuracy of our RV measurements, we observed 18 RV standards from the catalogue developed for the calibration of the Gaia Radial Velocity Spectrograph (Soubiran et al. 2013). Furthermore, we compare RVs from UVES spectra with RVs from GIRAFFE spectra, for a sample of stars in common between the two instruments. GIRAFFE observations are carried out with several setups HR03 (403-420 nm),

⁵ We quoted a statistical error $\sigma = 0.6 \text{ km s}^{-1}$ for the first internal data releases. This preliminary and more conservative estimate of the statistical error may have been used in some of the first science verification papers of the Gaia-ESO consortium.

HR05A (434-459 nm), HR06 (454-478 nm), HR09B (514-536 nm), HR10 (534-562 nm), HR14A (631-670), HR15N (647-679 nm), and HR21 (848-900 nm). We consider only stars observed with the HR15N (647-679 nm) setup to avoid the complications associated to the cross-calibration of different GIRAFFE setups and because most of the stars in common between the two instruments belongs to clusters, that have been observed only with this setup.

The list of RV standards observed during the first 18 months is reported in Table 1, while the bottom panel of Fig. 5 shows the distribution of the differences between the RVs measured with the two instruments. The RVs from the UVES spectra reported both in the table and in the plot are the average between the values calculated from the upper and the lower wavelength ranges. There is a systematic offset with respect to both the RVs of standards ($\langle RV_{UVES} - RV_{ST} \rangle = -0.47 \pm 0.14 \text{ km s}^{-1}$) and the RVs measured by the GIRAFFE pipeline for the spectra taken with the HR15N setup ($\langle RV_{UVES} - RV_{GIRAFFE} \rangle = -0.85 \pm 0.07 \text{ km s}^{-1}$). The offsets have the same sign, but the latter is significantly larger. This suggests that the RVs derived from both instruments need a more accurate zero point calibration. We are currently investigating how to improve the wavelength calibration, using the sky emission lines or the telluric features included in the spectra, and we are carrying out a comparison of RVs measured from all the different setups used for GIRAFFE and UVES to define a unique zero point for the Gaia-ESO Survey. Note that, as discussed by Worley et al. (2012), such small errors on the RVs do not affect the derivation of the stellar parameters.

The CCF_{FWHM} is correlated with the rotational velocity, so we can use the CCF computed for the determination of the RVs to estimate $v \sin i$. However, the CCF_{FWHM} also depends on the stellar parameters, which are not determined by our workflow, so the values of $v \sin i$ derived are only first guess estimations, that can be improved after the stellar parameters have been derived. To derive the relations between $v \sin i$ and the CCF_{FWHM} shown in Fig. 6, we created a set of rotationally broadened synthetic spectra, by convolving all the template spectra used for deriving the RVs with the rotational profile derived by Gray (2008). For each template, we created 12 spectra with $v \sin i$ ranging between 2 and 60 km s^{-1} and distributed on a logarithmic scale. Then, we run our procedure for the determination of the RVs on the whole set of rotationally broadened templates and from the results we derived a relation between CCF_{FWHM} and $v \sin i$. This relation was inverted to derive $v \sin i$ from the CCF_{FWHM} calculated for the observed stars. Errors on $v \sin i$ have been also calculated from the dispersion of the CCF_{FWHM} at fixed $v \sin i$ (see Fig. 6).

As said before, in order to have only one spectrum per star at the end of the survey, we co-added all the repeated observations. However, to avoid errors in the spectral analysis due to the presence of double-lined spectroscopic binaries or to single-lined spectroscopic binaries observed multiple times, we include in our final products two binarity flags: a) we perform a visual inspection of the $CCFs$ computed before co-adding multi-epoch observations, and flag a star as a candidate double-lined spectroscopic binary, if the $CCFs$ are characterized by the presence of more than one peak or a single peak with strong asymmetries; b) we classify a star as a single-lined spectroscopic binary if the median absolute deviation of multi-epoch repeated measurements of the RV is larger than twice the error on RV calculated as discussed above.

6. Quality control

We perform a quality control of the calibration frames and the spectra to check that the data reduction software is working correctly and that problems during the fiber allocation process do not affect the final quality of the spectra. Specifically, our procedure for quality control consists of three steps:

1. We store several output parameters from the ESO pipeline, which allow us to assess the stability of the BIAS frames (e.g., BIAS level), the accuracy of the table which defines the spectral format (e.g., root mean square of the shifts between the spectral format derived from a calibration frame and an analytical model of the spectral format), and the precision of the wavelength calibration (e.g., number of lines used and root mean square of the residuals of the wavelength solution). Whenever, during the data reduction process and the following steps of the quality control, we come across a problem (e.g. crash of the pipeline, artifacts in the spectra), we use these parameters to investigate the origin of the problem. In particular, we analyse if the parameters assume anomalous values with respect to the typical values observed during the survey or if they follow a trend. For this analysis, we also used the ESO Health Check Monitor for FLAMES-UVES (available at the website <http://www.eso.org/observing/dfo/quality/UVES/qc/qc1.html>), which allows us to compare the quality of the calibration frames used for processing the data of the survey with the typical quality of the FLAMES-UVES calibration frames.
2. We perform a visual quality control of all the spectra to check the presence of anomalies in the spectrum, like artificial noise, gaps and ripples. When we find such problems, we investigate if they originate from the science frame, the calibration frames or from the pipeline, and we evaluate possible actions to be taken, in some cases in collaboration with the ESO data reduction and user support team.
3. After each run, we compare the SNR per pixel of the observed spectra with the expected SNR from the ESO exposure time calculator. The SNR per pixel of the observed spectrum is calculated with the DER-SNR algorithm (Stoehr et al. 2008), which was developed to perform empirical and unbiased calculations of SNR on large datasets. When we observe significant discrepancies between the expected and the observed SNRs, we investigate if they are due to the data reduction or to the target selection process. Specifically, lower than expected SNRs may be due to artificial noise produced by the pipeline, low sky transparency, poor accuracy of the stellar astrometry and photometry. In the upper panels of Fig. 7 we compare the observed and predicted SNRs for all the stars with known V magnitude observed during the first 18 months of the Gaia-ESO Survey. For most of the stars there is a good agreement between the predicted and the expected SNR, which demonstrates that both the data reduction and the fiber allocation procedure have been carried out correctly. A small number of stars with lower than predicted SNR is expected, since not all the observations have been performed in conditions of clear sky. In the bottom panels of Fig. 7 we show the predicted and observed SNR as a function of wavelength for one star observed in good weather conditions (ID 18280330+0639516). The plot shows that our method to calculate the SNR from the observed spectra is consistent with the ESO exposure time calculator.

Table 1. Radial velocities of Gaia standard stars.

Star	RA (J2000)	DEC (J2000)	B-V (mag)	RV ^a (km s ⁻¹)	RV _{GES} ^b (km s ⁻¹)	RV _{GES} -RV (km s ⁻¹)	RV _{GESU} -RV _{GESL} /√2 (km s ⁻¹)
HIP017147	03:40:21.7	-03:12:59.3	0.55	120.400±0.0066	119.99	-0.41	0.02
HIP026973	05:43:26.4	-47:49:24.6	0.86	26.600±0.0057	26.30	-0.30	0.04
HIP029295	06:10:34.7	-21:51:46.5	1.49	4.892±0.0088	3.56	-1.33	0.45
HIP031415	06:35:03.0	-12:36:26.2	0.51	-7.479±0.0115	-7.71	-0.23	0.11
HIP032045	06:41:43.0	-33:28:11.1	1.05	40.722±0.0065	39.95	-0.77	0.11
HIP032103	06:42:23.4	-61:13:31.1	0.75	27.167±0.0062	27.36	0.19	0.04
HIP038747	07:55:58.2	-09:47:49.7	0.67	-8.002±0.0071	-8.39	-0.39	0.28
HIP045283	09:13:44.8	-42:18:37.0	0.58	39.451±0.0053	38.54	-0.91	0.19
HD88725	10:14:08.2	03:09:08.2	0.61	-21.976±0.0052	-22.49	-0.52	0.07
HIP51007	10:25:11.2	-10:13:44.4	1.46	21.758±0.0064	21.01	-0.75	0.61
HIP058345	11:57:56.9	-27:42:19.9	1.13	48.605±0.0088	47.47	-1.14	0.25
HIP65859	13:29:59.1	10:22:47.2	1.49	14.386±0.0087	13.79	-0.60	0.37
HIP077348	15:47:24.2	-01:03:48.6	0.79	1.907±0.0114	2.42	0.52	0.21
HIP104318	21:07:56.4	07:25:58.7	0.69	4.910±0.0059	3.91	-1.00	0.12
HIP105439	21:21:23.7	-51:45:08.6	0.65	17.322±0.0062	17.33	0.01	0.25
HD204587	21:30:02.2	-12:30:34.0	1.26	-84.533±0.0092	-85.58	-1.05	0.51
HIP108065	21:53:41.7	-28:40:12.3	0.73	-41.660±0.0100	-42.30	-0.64	0.07
HIP113576	23:00:16.7	-22:31:28.2	1.38	16.138±0.0095	17.04	0.90	0.89

Notes. Radial velocities of stars included in the catalogue of standards for the calibration Gaia Radial Velocities Spectrometer (Soubiran et al. 2013)

^(a) Radial velocity from Soubiran et al. 2013.

^(b) Average of the radial velocities of the lower and upper spectrum derived by pipeline used to process FLAMES-UVES spectra.

Our quality control procedure and the fruitful collaboration with the ESO data reduction group allowed us to solve most of the problems of the data reduction process. However, minor issues that need to be solved still affect $\sim 4 - 5\%$ of the spectra. Specifically, the merged spectra of bright stars are affected by ripples in the wavelength ranges in common between two orders and, in a small minority of cases, the sky spectrum below 5000 Å is overestimated, so the final spectrum is oversubtracted in this wavelength range. To avoid that these minor issues may affect the analysis, the output files include the spectra from each single order and the subtracted sky spectrum.

7. Data products

Our products are periodically released to the WGs⁶, which perform the spectral analysis and on different timescales to ESO, which releases them to the general astronomical community by its public website (http://www.eso.org/sci/observing/phase3/data_releases.html). All our products are organized in multi-extension FITS files. We provide three different categories of output files: a) files including all the spectra from a single exposure; b) files including all the co-added spectra from multiple exposures of the same OB and/or different OBs with the same stars, same setup, and observed during the same night; c) files including only the spectrum of one star, resulting from the stacking of all the spectra of that star observed with the same setup during the whole survey. All the output files include:

- A spectrum obtained by merging all the spectral orders together, before the normalisation, with its variance.

- A normalized version of the above spectrum, with its variance.
- All the single spectral order spectra before merging, with their variances.
- The spectrum of the sky used for the subtraction.
- The function used for the continuum normalisation.
- The CCF used for deriving the RV and $v \sin i$ as discussed in Sect. 5.
- A table including information about the stars (e.g. coordinates, name, magnitude), information about the spectra (e.g. SNR⁷, root mean square of the residuals of the wavelength solution), the RV with error, the template used to derive the RV, properties of the CCF (e.g. width and height of the peak), $v \sin i$ with error, RV quality flag and binarity flags.
- The final files with stacked spectra also include the original spectra before co-adding and specific information on each of them.
- Information on the observations (e.g. data, name of the observing block, seeing, airmass) are reported in the header of the files.

8. Summary

This work is part of a series of papers aimed at describing methods, software and procedures used for the Gaia-ESO Survey. Specifically, we describe the data reduction and the determination of RVs for the FLAMES-UVES spectra. We can summarize the content of this work as follows:

1. The basic steps of the data reduction process (bias subtraction, flat-fielding, wavelength calibration, spectra extraction)

⁶ The spectra are released to the other WGs of the Gaia-ESO consortium with an operational database developed by the Cambridge Astronomical Survey Unit (CASU) based at the Institute of Astronomy at the University of Cambridge (see <http://casu.ast.cam.ac.uk/gaiaeso/>).

⁷ In the fits table we report a median of the SNR for the whole wavelength range. This value is different from what reported in Fig. 7, where the SNR is calculated in a small wavelength range to allow us a better comparison with the predicted values.

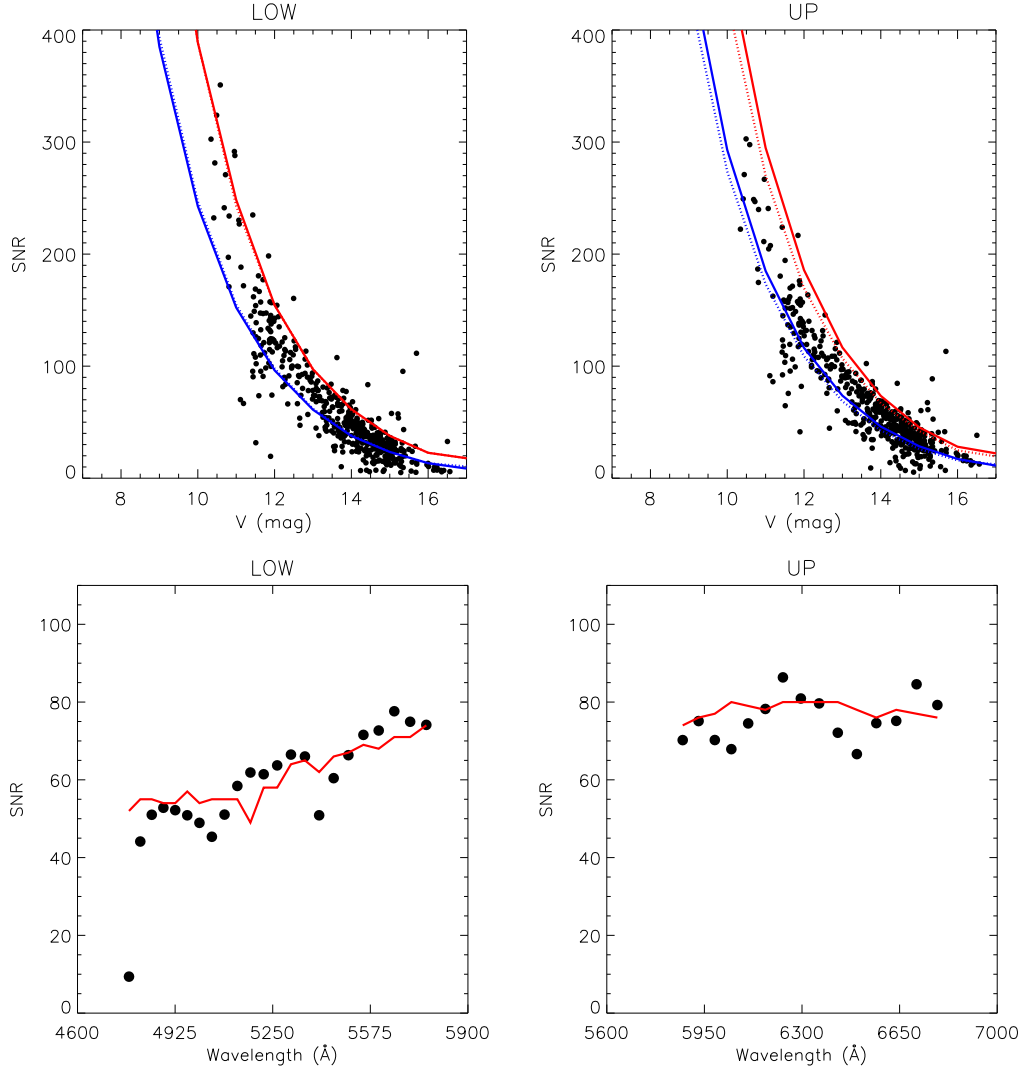


Fig. 7. Top panels: Comparison between predicted (continuous lines) and measured (black dots) SNRs for the stars observed during the first 18 months of the survey, with known V magnitude from the literature or from public archives. The upper and lower spectra are shown in the left and right panels, respectively. The lines show the predicted SNR calculated by the ESO exposure time calculator (vers. 5.0.1) in the 5470-5520 Å (left panel) and the 6250-6320 Å (right panel) spectral ranges, considering an exposure time of 3000 s, airmass of 1.2, the input spectra of a K2 (continuous line) and a G0 (dotted line) star and two values of seeing 0.66'' (red line) and 1.57'' (blue line), which correspond to the 10th and 90th percentile ranks of the seeing measured during the observations. The black dots represent the SNRs of the observed spectra measured in the same wavelength range using the DER SNR algorithm (see Sect. 6) and scaled to the exposure time of 3000 s, assuming that the SNR is photon limited (i.e., $\text{SNR} \propto \sqrt{\text{exposure time}}$). **Bottom panels:** Comparison between predicted (continuous red line) and measured SNRs (black dots) as a function of wavelength for the star 18280330+0639516. The lower and upper wavelength ranges are shown in the left and in the right panels, respectively.

are carried out with a workflow specifically developed to run the ESO public pipeline in the most efficient way for the reduction of the spectra of the Gaia-ESO Survey.

2. We perform preliminary steps (i.e. barycentric correction, sky-subtraction, spectral co-adding and normalisation) of the data analysis with a pipeline based on pyraf and IDL.
3. We derive RVs and $v \sin i$ by cross-correlating all the spectra with a sample of synthetic templates. The typical error on RVs is $\sigma \sim 0.4 \text{ km s}^{-1}$ and the major source of error is the variation of the zero point of the wavelength calibration. A comparison with the RVs measured using GIRAFFE spectra indicate the presence of a systematic offset of $\sim 0.9 \text{ km s}^{-1}$ between the two instruments. We are investigating how to improve the precision and the accuracy of the RVs (e.g. by using sky lines) and we are carrying out an overall assess-

ment of the zero point shifts of all the instruments and setups to put all the RVs of the Gaia-ESO Survey on the same zero point.

4. We perform a detailed quality control of our final products, which is based on the analysis of the output parameters from the ESO pipeline, a visual inspection of the spectra and an analysis of the SNR.
5. Our output is organized in multi-extension FITS files, which include both spectra at various stages of the data reduction process (e.g. normalized, not normalized, co-added, not co-added), and various information on the spectra, which are collected in tables (e.g. coordinates, RVs, magnitudes).

Acknowledgements. We acknowledge the support from INAF and Ministero dell'Istruzione, dell'Università e della Ricerca (MIUR) in the form of the grant "Premiale VLT 2012". The results presented here benefit from discussions held

during the Gaia-ESO workshops and conferences supported by the ESF (European Science Foundation) through the GREAT Research Network Programme. This work was partly supported by the European Union FP7 programme through ERC grant number 320360 and the Leverhulme Trust through grant RPG-2012-541. We acknowledge financial support from "Programme National de Cosmologie and Galaxies" (PNCG) of CNRS/INSU, France.

References

- de Laverny, P., Recio-Blanco, A., Worley, C. C., & Plez, B. 2012, *A&A*, 544, A126
- Fitzpatrick, M. J. 1993, in *Astronomical Society of the Pacific Conference Series*, Vol. 52, *Astronomical Data Analysis Software and Systems II*, ed. R. J. Hanisch, R. J. V. Brissenden, & J. Barnes, 472
- Gilmore, G., Randich, S., Asplund, M., et al. 2012, *The Messenger*, 147, 25
- Gray, D. F. 2008, *The Observation and Analysis of Stellar Photospheres*, 3rd edn. (Cambridge University Press)
- Modigliani, A. & Larsen, J. M. 2012, *FLAMES-UVES pipeline user manual*, 14th edn., ESO
- Modigliani, A., Mulas, G., Porceddu, I., et al. 2004, *The Messenger*, 118, 8
- Mulas, G., Modigliani, A., Porceddu, I., & Damiani, F. 2002, in *Proc. of SPIE*, Vol. 4844, *Observatory Operations to Optimize Scientific Return III*, ed. P. J. Quinn, 310
- Pasquini, L., Avila, G., Blecha, A., et al. 2002, *The Messenger*, 110, 1
- Randich, S. & Gilmore, G. 2013, *The Messenger*, 154, 47
- Soubiran, C., Jasiewicz, G., Chemin, L., et al. 2013, *A&A*, 552, A64
- Stoehr, F., White, R., Smith, M., et al. 2008, in *Astronomical Society of the Pacific Conference Series*, Vol. 394, *Astronomical Data Analysis Software and Systems XVII*, ed. R. W. Argyle, P. S. Bunclark, & J. R. Lewis, 505
- Tody, D. 1986, in *Proc. of SPIE*, Vol. 627, *Instrumentation in astronomy VI*, ed. D. L. Crawford, 733
- Tody, D. 1993, in *Astronomical Society of the Pacific Conference Series*, Vol. 52, *Astronomical Data Analysis Software and Systems II*, ed. R. J. Hanisch, R. J. V. Brissenden, & J. Barnes, 173
- Worley, C. C., de Laverny, P., Recio-Blanco, A., et al. 2012, *A&A*, 542, A48
- ¹ INAF-Osservatorio Astrofisico di Arcetri, Largo E. Fermi, 5, 50125, Firenze, Italy
- ² European Southern Observatory, Karl-Schwarzschild-Strasse 2, 85748 Garching bei München, Germany
- ³ Institute of Astronomy, University of Cambridge, Madingley Road, Cambridge CB3 0HA, United Kingdom
- ⁴ Research School of Astronomy & Astrophysics, Australian National University, Cotter Road, Weston Creek, ACT 2611, Australia
- ⁵ Rudolf Peierls Centre for Theoretical Physics, Keble Road, Oxford, OX1 3NP, United Kingdom
- ⁶ GEPI, Observatoire de Paris, CNRS, Université Paris Diderot, 5 Place Jules Janssen, 92195 Meudon, France
- ⁷ Centre for Astronomy Research, University of Hertfordshire, Hatfield, Hertfordshire, AL10 9AB United Kingdom
- ⁸ Lund Observatory, Department of Astronomy and Theoretical Physics, Box 43, SE-221 00 Lund, Sweden
- ⁹ Institute of Astronomy, University of Edinburgh, Blackford Hill, Edinburgh EH9 3HJ, United Kingdom
- ¹⁰ Astrophysics Group, Research Institute for the Environment, Physical Sciences and Applied Mathematics, Keele University, Keele, Staffordshire ST5 5BG, United Kingdom
- ¹¹ INAF - Osservatorio Astronomico di Palermo, Piazza del Parlamento 1, 90134, Palermo, Italy
- ¹² Departamento de Física, Ingeniería de Sistemas y Teoría de la Señal, Universidad de Alicante, Apdo. 99, 03080, Alicante, Spain
- ¹³ ESA, ESTEC, Keplerlaan 1, Po Box 299 2200 AG Noordwijk, The Netherlands
- ¹⁴ Max-Planck Institut für Astronomie, Königstuhl 17, 69117 Heidelberg, Germany
- ¹⁵ INAF - Padova Observatory, Vicolo dell'Osservatorio 5, 35122 Padova, Italy
- ¹⁶ Instituto de Astrofísica de Andalucía-CSIC, Apdo. 3004, 18080, Granada, Spain
- ¹⁷ Instituto Astrofísica de Canarias, 38205, La Laguna, Tenerife, Spain
- ¹⁸ Universidad de La Laguna, Depart. de Astrofísica, 38206, La Laguna, Tenerife, Spain
- ¹⁹ Lund Observatory, Department of Astronomy and Theoretical Physics, Box 43, SE-221 00 Lund, Sweden
- ²⁰ Royal Observatory of Belgium, Ringlaan 3, 1180, Brussels, Belgium
- ²¹ INAF - Osservatorio Astronomico di Bologna, via Ranzani 1, 40127, Bologna, Italy
- ²² Institute of Astronomy, University of Edinburgh, Blackford Hill, Edinburgh EH9 3HJ, United Kingdom
- ²³ Department of Physics and Astronomy, Division of Astronomy and Space Physics, Uppsala University, Box 516, SE-75120 Uppsala, Sweden
- ²⁴ Dipartimento di Fisica e Astronomia, Sezione Astrofisica, Università di Catania, via S. Sofia 78, 95123, Catania, Italy
- ²⁵ ASI Science Data Center, Via del Politecnico SNC, 00133 Roma, Italy
- ²⁶ Laboratoire Lagrange (UMR7293), Université de Nice Sophia Antipolis, CNRS, Observatoire de la Côte d'Azur, CS 342293, F-06304 Nice cedex 4, France
- ²⁷ Department for Astrophysics, Nicolaus Copernicus Astronomical Center, ul. Rabiańska 8, 87-100 Toruń, Poland
- ²⁸ Institut d'Astronomie et d'Astrophysique, Université libre de Bruxelles, Boulevard du Triomphe, 1050 Brussels, Belgium
- ²⁹ European Southern Observatory, Karl-Schwarzschild-Str. 2, 85748 Garching bei München, Germany